

# Dislocations in bilayer graphene

Benjamin Butz<sup>1</sup>, Christian Dolle<sup>1</sup>, Florian Niekiel<sup>1</sup>, Konstantin Weber<sup>2</sup>, Daniel Waldmann<sup>3</sup>, Heiko B. Weber<sup>3</sup>, Bernd Meyer<sup>2</sup> & Erdmann Spiecker<sup>1</sup>

Dislocations represent one of the most fascinating and fundamental concepts in materials science<sup>1-3</sup>. Most importantly, dislocations are the main carriers of plastic deformation in crystalline materials<sup>4-6</sup>. Furthermore, they can strongly affect the local electronic and optical properties of semiconductors and ionic crystals<sup>7,8</sup>. In materials with small dimensions, they experience extensive image forces, which attract them to the surface to release strain energy9. However, in layered crystals such as graphite, dislocation movement is mainly restricted to the basal plane. Thus, the dislocations cannot escape, enabling their confinement in crystals as thin as only two monolayers. To explore the nature of dislocations under such extreme boundary conditions, the material of choice is bilayer graphene, the thinnest possible quasi-two-dimensional crystal in which such linear defects can be confined. Homogeneous and robust graphene membranes derived from high-quality epitaxial graphene on silicon carbide10 provide an ideal platform for their investigation. Here we report the direct observation of basal-plane dislocations in freestanding bilayer graphene using transmission electron microscopy and their detailed investigation by diffraction contrast analysis and atomistic simulations. Our investigation reveals two striking size effects. First, the absence of stacking-fault energy, a unique property of bilayer graphene, leads to a characteristic dislocation pattern that corresponds to an alternating AB  $\leftrightarrow$  AC change of the stacking order. Second, our experiments in combination with atomistic simulations reveal a pronounced buckling of the bilayer graphene membrane that results directly from accommodation of strain. In fact, the buckling changes the strain state of the bilayer graphene and is of key importance for its electronic properties<sup>11-14</sup>. Our findings will contribute to the understanding of dislocations and of their role in the structural, mechanical and electronic properties of bilayer and few-layer graphene.

In graphite, the bulk material most closely related to graphene, basal-plane dislocations have been well known since the early 1960s<sup>15</sup>. The dissociation of perfect basal-plane dislocations into pairs of Shockley partial dislocations (partials) bounding a stacking-fault ribbon in the basal plane was observed using conventional transmission electron microscopy<sup>15,16</sup> (TEM). The separation of partials (or the width of the stacking-fault ribbon) is determined by the balance between the repulsive forces (reduction of total strain energy) and the attractive forces (minimization of stacking-fault energy). Similarly, the dissociation of perfect dislocations into Shockley partials plays an essential role for most materials with face-centred-cubic structure and is of particular importance for the plasticity of face-centred-cubic metals<sup>9</sup>.

Also in few-layer graphene, changes of the stacking sequence have been reported <sup>17–22</sup>. For instance, dark-field TEM was used to reveal changes in the stacking order and twisting of freestanding bi- and trilayer graphene grown by chemical vapour deposition <sup>18</sup> (CVD). However, the partials necessarily connected to the stacking faults were not addressed in that study. Moreover, scanning tunnelling microscopy was used to investigate local changes in the stacking sequence of few-layer graphene on mica <sup>19</sup>. The boundaries, which separate areas of different stacking order, form a pattern that closely resembles dislocation networks in bulk graphite,

indicating that it may be possible to study basal-plane dislocations in few-layer graphene. Two recent publications  $^{17,20}$  address in more detail the local stacking transition  $AB \leftrightarrow AC$  in bilayer graphene grown by CVD (subsequently stacked  $^{17}$  or as-grown  $^{20}$ ). In both studies, the authors applied dark-field TEM to investigate the local bilayer graphene stacking and to characterize the distribution of the transition regions. Moreover, atomistic models were derived from comparison with high-resolution scanning TEM (STEM) images. The transition regions were described either in terms of strain solitons using a Frenkel–Kontorova model  $^{17}$  or with complicated atomistic models, including the delamination of the two graphene layers, which were proposed, on the basis of molecular dynamics simulation, to explain the experimental data  $^{20}$ . However, none of this work describes the transition regions in terms of classical dislocation theory.

Important modifications of dislocations are expected when going from graphite to freestanding few-layer graphene membranes. First, pronounced buckling of the membrane is expected as a result of strain accommodation. Moreover, in bilayer graphene the unique situation occurs that both stacking variants, AB and AC (or BA, which means the same), are equivalent. This means that no stacking-fault energy exists and, therefore, that no attractive forces act between partials to reduce the stacking-fault area.

In the following, we present the detailed microscopic study of basalplane dislocations in bilayer graphene membranes prepared from highquality epitaxial graphene on the (0001) surface of 6H-SiC (ref. 10; throughout the manuscript four Bravais–Miller indices are used to account for the hexagonal symmetry). The central region of a typical TEM sample with more than 150 membranes is shown in Fig. 1a. The colour-coded STEM image of one membrane (Fig. 1b) indicates the local variation in the number of graphene layers as determined by Raman microscopy<sup>10</sup> and TEM (see below). Apart from the bilayer

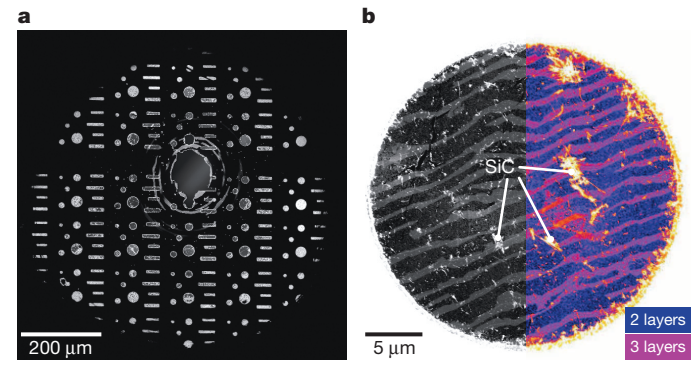


**Figure 1** | Freestanding bilayer graphene membranes in a SiC frame. **a**, Dark-field STEM image (obtained in a scanning electron microscope) of a sample with circular and rectangular membranes. The non-transparent SiC is dark and the freestanding membranes appear bright. **b**, Single membrane at higher magnification. The colour code indicates the local number of graphene layers (compare with ref. 10).

<sup>&</sup>lt;sup>1</sup>Center for Nanoanalysis and Electron Microscopy, Friedrich-Alexander-Universität Erlangen-Nürnberg, Cauerstraße 6, 91058 Erlangen, Germany. <sup>2</sup>Interdisziplinäres Zentrum für Molekulare Materialien und Computer-Chemie-Centrum, Friedrich-Alexander-Universität Erlangen-Nürnberg, Nägelsbachstraße 25, 91052 Erlangen, Germany. <sup>3</sup>Lehrstuhl für Angewandte Physik, Friedrich-Alexander-Universität Erlangen-Nürnberg, Staudtstraße 7, 91058 Erlangen, Germany.

graphene, the membranes exhibit regions consisting of three (or even four) graphene layers.

To study the microstructure and crystal defects in the graphene membrane, we employed dark-field TEM imaging. Figure 2a shows a  $\{11\overline{2}0\}$  dark-field image of a typical membrane area with predominantly bilayer graphene and a smaller portion of trilayer graphene. The bilayer and trilayer nature of the corresponding areas is confirmed by a detailed rocking-curve analysis based on a  $\{11\overline{2}0\}$  dark-field tilt series (Fig. 2c, Extended Data Fig. 2 and Supplementary Video 1).

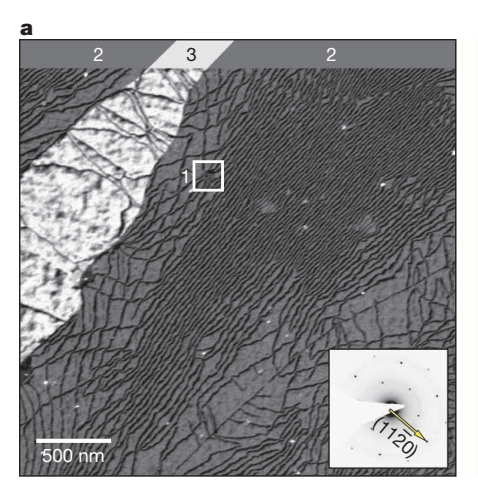
In the following, we concentrate on the bilayer region. Most notably, a dense network of dislocations, confined between the two graphene sheets, appears as relatively sharp dark lines in Fig. 2a. As confirmed by the detailed Burgers vector analysis (see below), all the dislocations are partials, meaning that their Burgers vectors are of type  $b=(1/3)\langle 1\bar{1}00\rangle$  and therefore do not correspond to lattice translations in the basal plane. Thus, each partial is associated with a change of the local stacking between AB and AC, or vice versa. This is shown in the corresponding  $(2\bar{2}00)$  dark-field image in Fig. 2b, where the two stacking orders in the bilayer regions appear with different intensities.

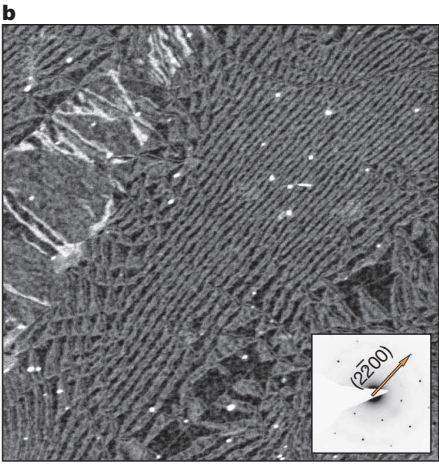
All this is congruent with dislocation theory in materials science, where stacking faults in three-dimensional (3D) crystals are always bordered by partials. However, the essential difference is that the stacking-fault energy in bilayer graphene is zero because AB and AC are equivalent by symmetry; in other words, a non-zero stacking-fault energy arises only if a third graphene layer is added. In line with this consideration, Fig. 2b shows that the two stacking variants occupy about equal portions of the bilayer area (in contrast to the trilayer region). Single partials in trilayer graphene directly cause a change in the crystal structure, for example from Bernal stacking to rhombohedral stacking (ABA  $\leftrightarrow$  ABC), resulting in real stacking faults<sup>17-22</sup> (compare the respective trilayer regions in Figs 2b and 3b). Apart from regions with an apparently irregular distribution of dislocations, for example close to the trilayer region in Fig. 2a, we found that a large fraction of our bilayer graphene exhibited parallel aligned partials (see, for example, the centre of Fig. 2a). The typical spacing between individual partials in such regions is in the range of 20-30 nm. Concerning the origin of the dislocations, TEM

studies of membranes covering very small substrate holes (Extended Data Fig. 3) indicate that a large portion of the dislocations must already be present in the graphene on the SiC wafer before the substrate is removed. We assume that the dislocations form as result of misfit stresses either during the growth of the graphene on the SiC or while the samples are cooled from  $1,750\,^{\circ}\text{C}$  to room temperature (owing to different thermal expansion coefficients).

The central region of Fig. 2a with the characteristic equidistant arrangement of parallel dislocations was selected to analyse the Burgers vectors and strain fields of the partials in detail. By systematic dark-field imaging with specific  $\{11\bar{2}0\}$  and  $\{1\bar{1}00\}$  reflections, the dislocations are unambiguously identified as  $60^\circ$  partials with alternating Burgers vectors of type  $b=(1/3)\langle 1\bar{1}00\rangle$  (Fig. 3). This result matches the alteration of the stacking sequence (AB  $\leftrightarrow$  AC  $\leftrightarrow$  AB) as observed in Fig. 2b. As a consequence, each pair of partials (in the homogeneous bilayer regions) results in a perfect lattice translation along  $\langle 11\bar{2}0\rangle$  corresponding to an effective perfect edge dislocation.

To explore the peculiarities of basal-plane dislocations in bilayer graphene, we carried out atomistic simulations of the equidistant arrangement of partials. Starting with a perfect edge dislocation, splitting into equidistant 60° partials occurs during structural optimization (Fig. 4a). This is in agreement both with our experimental observation and with energetic arguments based on the absence of stacking-fault energy. Apart from the alteration of the stacking (Fig. 4a, top view), the most notable feature is the pronounced buckling (by around 1 nm) of the membrane (Fig. 4a, 3D visualization and side view). Unlike the wellknown intrinsic corrugations of perfect monolayer graphene<sup>23</sup>, this buckling is directly associated with the dislocation lines because the driving force for the buckling is release of strain energy in the dislocation strain field. To understand the impact of buckling on the strain state, we compare the buckled configuration (Fig. 4a) with a flat one, where the movement of the atoms during the atomic relaxation was restricted to the x-y plane. The latter configuration can be thought to represent bilayer graphene on a flat compliant substrate, for example a wafer with an appropriate amorphous surface layer.





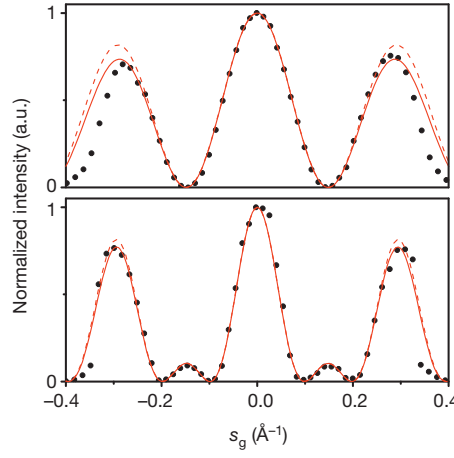


Figure 2 | Microstructure analysis by dark-field TEM imaging. a, b, Dark-field TEM images of the same area of a membrane obtained with the  $(11\bar{2}0)$  and  $(2\bar{2}00)$  reflections. The diffraction patterns indicate the active reflection for dark-field imaging (SEM overview and respective bright-field images are given in Extended Data Fig. 1). The  $(11\bar{2}0)$  dark-field image (a) reveals bilayer and trilayer graphene as indicated by the numbers. The dark lines in the bilayer/ trilayer regions correspond to an extended network of partials confined between the graphene layers (see Fig. 3 for details). The line contrast results from the altered diffraction in the strain/displacement field of the dislocations. Because the  $\{11\bar{2}0\}$  reflections show identical structure factors (and rocking curves) for both stacking variants, AB and AC<sup>18</sup>, the stacking faults bordered by the partials are invisible irrespective of the sample tilt. The local transition of the stacking sequence in the bilayer graphene from AB to AC, and vice versa,

caused by partials observed in **a**, is clearly visible as areal intensity variation in the  $(2\bar{2}00)$  dark-field image (**b**). Unlike the  $\{11\bar{2}0\}$  reflections in **a**,  $\{1\bar{1}00\}$  and  $\{2\bar{2}00\}$  reflections show different rocking curves for AB and AC stacking <sup>18</sup>, meaning that small deviations from the Bragg condition lead to stacking-fault contrast as seen in the image. **c**, Rocking curves of  $\{11\bar{2}0\}$  dark-field intensities (in arbitrary units, a.u.) in dislocation-free areas of bi- and trilayer graphene (black dots) confirming the local number of graphene layers (see Extended Data Fig. 2 for details). The red lines are calculated rocking curves for bi- and trilayer graphene (equilibrium interlayer distance of 3.370 Å) taking the atomic scattering factor of carbon (dashed line) plus thermal damping (solid line) into account (see Extended Data Fig. 2 for details). The abscissa shows the excitation error  $s_g$ , which is related to the tilt angle and thus characterizes the scattering condition for each respective dark-field image.

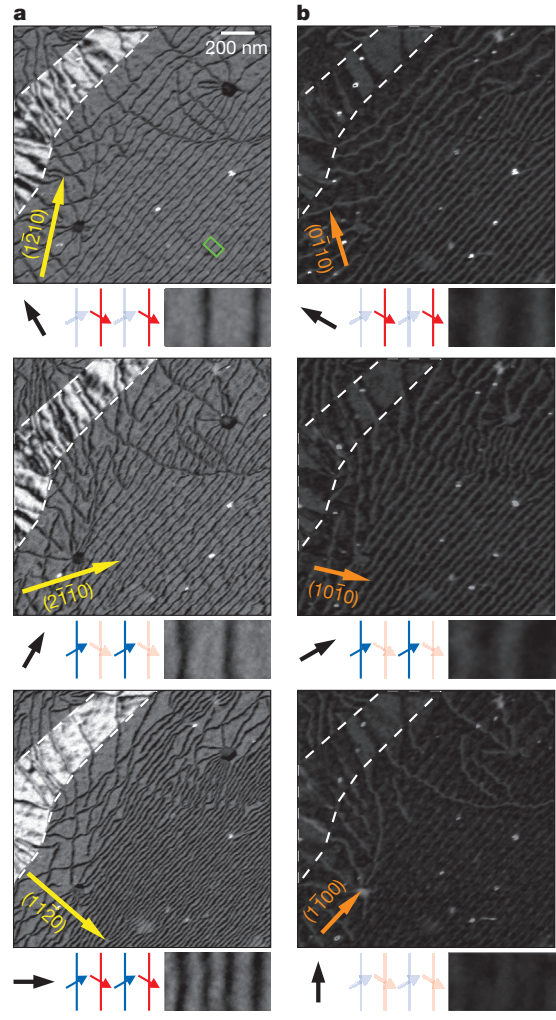


Figure 3 | Burgers vector analysis. a, b, Series of  $\{11\overline{2}0\}$  (a) and  $\{1\overline{1}00\}$ (b) dark-field images of the same region as in Fig. 2a (the corresponding diffraction pattern is given in Extended Data Fig. 4). The {1120} reflections (a) have a large structure factor for both AB and AC stacking<sup>18</sup> owing to the constructive interference for all atoms, such that relative shifts of the two graphene sheets in the displacement field of the dislocation lowers the local diffracted intensity. Therefore, the dislocations appear as dark lines on a bright background. In contrast, for  $\{1\overline{1}00\}$  dark-field images (b), they appear as bright lines on a dark background because the structure factor for such reflections is small owing to partial destructive interference of scattering waves from atoms in the A and B planes, as a result of which enhanced intensity is obtained in the displacement field of the dislocations. In contrast to  $\{2\overline{2}00\}$  dark-field images (Fig. 2b), the  $\{1\bar{1}00\}$  dark-field images do not show pronounced stacking-fault contrast because the deviation from the Bragg condition is too small for normal incidence. The diagram below each image shows the Burgers vector analysis, that is, a comparison of {1120} dark-field images of the same parallel dislocations (green box and magnified sections below the images). In the first two images only every second dislocation is visible (the ones that are seen in the first image are absent from the second one, and vice versa), whereas the third image shows both. Left of the enlarged dark-field images are schematic diagrams of the orientation relation between the respective diffraction vectors *g* (black arrow) and Burgers vectors *b* (red and blue arrows). By applying the  $g \cdot b = 0$  invisibility criterion, the two dislocation types are identified as  $60^{\circ}$  partials with Burgers vectors  $b_1 = (1/3)[10\overline{1}0]$  (blue) and  $b_2 = (1/3)[01\overline{1}0]$  (red). On the basis of these Burgers vectors, the contrast of the {1100} dark-field images (**b**) is understood as well. Dislocations show up with relatively strong contrast if *g* and *b* are parallel or antiparallel ( $|g \cdot b| = 2/3$ ), whereas they almost vanish if the angle between g and b is  $60^{\circ}$  ( $|g \cdot b| = 1/3$ ). Applying this finding to our reference region, only one variant of the partials shows up in the top two {1100} dark-field images, whereas only faint or residual contrast is seen in the third dark-field image. In  ${\bf b}$ , the areal contrast variations in the trilayer region, marked by dashed lines, are due to changes of the stacking sequence from ABA (bright) to ABC (dark).

Before discussing the phenomenon of strain accommodation in detail, we make comparison with the TEM experiments to validate the model and to confirm the Burgers vector analysis. In this relation, dark-field images were calculated using both atomistic configurations (buckled and flat). Figure 4b compares the experimental and simulated dislocation contrast in  $\{11\bar{2}0\}$  dark-field images (other reflections are shown in Extended Data Fig. 4). Within the accuracy of the experiment (owing to residuals on the membrane, the contrast varies slightly between the dislocations), there is very good agreement between experiment and simulation (especially using the buckled atomic configuration; see Fig. 4b). In particular, the applicability of the  $g \cdot b = 0$  invisibility criterion for determination of the Burgers vector is confirmed.

Most remarkably, the dislocation-induced buckling of the bilayer graphene could be validated by comparing the second-order derivative calculated from experimental images (Fig. 4c, lower part) with the respective distributions obtained from both simulations (Fig. 4c, upper part). The same curvature (given by the second derivative) at the intensity maxima and minima of the original ( $11\bar{2}0$ ) dark-field image, reflected in bright lines with similar intensities in the modulus of the second derivative, is an excellent fit to the prediction of our simulation with the buckled atomic configuration. Prospectively, membranes with improved quality will allow for a more precise evaluation of the intensity distribution across single dislocations, enabling both the optimization of the theoretical interaction potential between graphene layers and the determination of the Peierls potential of the dislocations. These results will help to explain the mechanical properties of bilayer and few-layer graphene.

Figure 4d and Fig. 4e compare the respective profiles of the in-plane strain components,  $\varepsilon_{xx}$ ,  $\varepsilon_{yy}$  and  $\varepsilon_{xy}$  for the two layers in both configurations. It can be seen that the buckling completely alters the strain state of the two graphene layers. In the flat configuration, the normal strain component,  $\varepsilon_{xx}$ , shows pronounced maxima and minima at the dislocations cores (localized tension and compression of the graphene layers), whereas the same strain component almost completely levels out on buckling, resulting in a small and uniform strain (tensile in the lower layer but compressive in the upper layer) across the whole bilayer graphene ribbon. For symmetry reasons,  $\varepsilon_{yy}$  is almost zero for the two layers (in both configurations). Unexpectedly, the shear component,  $\varepsilon_{xy}$  is much more localized in the buckled configuration. As a result, both the local disregistry, that is, the relative shift of the two layers, and the Burgers vector distributions are completely different for the buckled and the flat configurations (compare the respective distributions in the bottom parts of Fig. 4d and Fig. 4e).

Our simulations demonstrate how sensitively the strain state and the local stacking of the two graphene layers depend on the topography of the bilayer graphene. This is of great interest because one key aim of the field is to engineer a suitable bandgap for applications using strained bilayer or few-layer graphene. However, the dislocation-induced local buckling and, in particular, the resulting strain redistribution have been neglected in the literature so far<sup>14,17,20</sup>.

It is worth comparing the basal-plane dislocations in bilayer graphene with dislocations in monolayer graphene (see, for example, refs 24-26) and putting both in the context of classical dislocation theory. At first glance, the two types of dislocations seem fundamentally different. Whereas the former lie in the plane of the membrane and can be as long as several micrometres, the dislocations in monolayer graphene possess an infinitesimally short dislocation line perpendicular to the graphene membrane (making even the definition of a dislocation line questionable) and thus seem more like topological defects in a two-dimensional (2D) crystal. However, in both cases the membranes are embedded in 3D space, allowing for strain relief in the third dimension by, for example, buckling (see, for example, refs 25, 27 for monolayer graphene). In fact, dislocations intersecting a thin plate in the normal direction were studied in elasticity theory more than 60 years ago<sup>28</sup>. The focus was on screw dislocations (for which there is no equivalent in monolayer graphene), but in relation to edge dislocations it was stated that in "certain circumstances an edge dislocation will be able to relieve most of its stress by slight

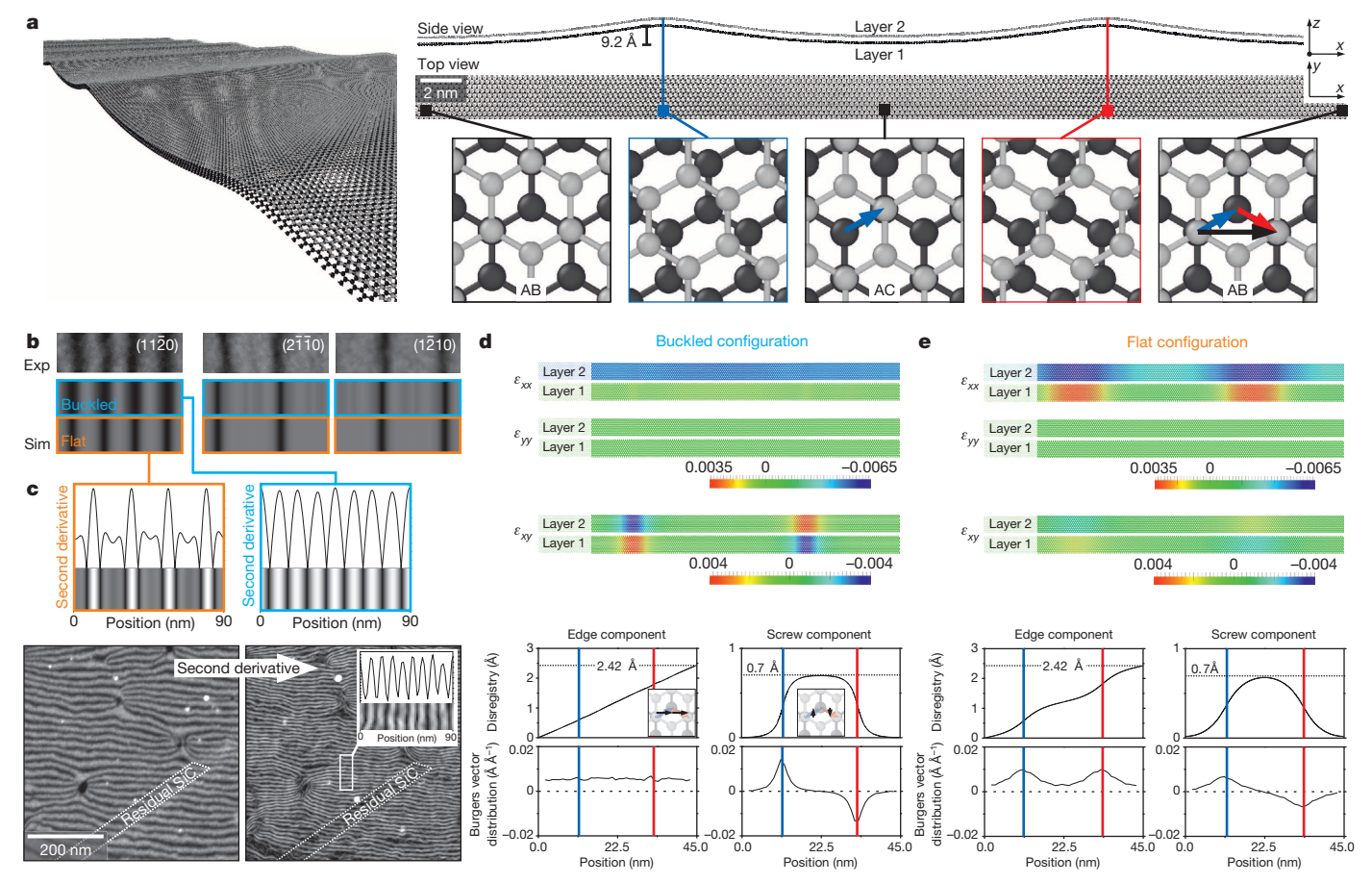


Figure 4 | Atomistic simulation of 60° partial dislocations: atomic configuration, TEM simulation, strain distribution and Burgers vector **distribution.** a, Atomistic simulation of a pair of parallel 60° partials as observed in our bilayer graphene (compare with Fig. 3): 3D visualization, side view, top view. The blue and red lines mark the dislocation cores. The gradual change of the stacking sequence,  $AB \leftrightarrow AC \leftrightarrow AB$ , across the two partials is shown enlarged together with the corresponding Burgers vectors of type  $(1/3)(1\bar{1}00)$  (blue and red). The total relative shift (black vector) amounts to one lattice translation along the *x* direction (total Burgers vector of type  $(1/3)\langle 11\overline{2}0\rangle$ ; for example,  $(1/3)[10\overline{1}0] + (1/3)[01\overline{1}0] = (1/3)[11\overline{2}0]$ ). The local bond lengths and angles are depicted in Extended Data Fig. 6. b, Comparison of experimental {1120} dark-field images (compare with Fig. 3) with simulated ones that are based on the buckled configuration in a (blue outline) and, as reference, a flat one (orange outline). The specific strain states of these atomic configurations cause different intensity distributions across the dislocations in dark-field imaging. In particular, the widths of the respective intensity minima are remarkably different for the two configurations, most notably in the  $(11\bar{2}0)$ 

dark-field images, in which the edge components of both dislocations are directly probed (further dark-field images with other reflections are depicted in Extended Data Fig. 4). c, Proof of local buckling using the second derivative of the dark-field intensity distributions. The second-derivative profiles (obtained from b), the absolute values of which are plotted in the upper part, are distinctively different for the buckled and the flat configurations. Applying the same procedure to experimental (1120) dark-field images (lower part) validates our buckled atomistic configuration. The inset in the second derivative of the experimental image depicts a representative intensity profile (averaging over 3 pixels) with characteristic variations. d, e, Atomistic strain components,  $\varepsilon_{xx}$ ,  $\varepsilon_{xy}$  and  $\varepsilon_{yy}$ , for the two layers of the buckled configuration (**d**) and for those of the flat reference configuration (e), where the movement of the atoms during optimization was restricted to the x-y plane (fixed z coordinate). The distributions are shown together with the disregistry, that is, the relative shift of the two graphene layers, and the Burgers vector distributions for the edge and screw components of the partials.

buckling of the plate". Along similar lines, the buckling of a thin foil due to dislocations lying in the plane of the foil (such as our basal plane dislocations in bilayer graphene) has also been investigated<sup>29</sup>. As in our case, the buckling is caused by an in-plane edge component of the Burgers vector. Thus, both the edge dislocations in monolayer graphene and the basal-plane dislocations in bilayer graphene can be viewed as limiting cases of classical dislocations in thin plates.

We have studied basal-plane dislocations in freestanding bilayer graphene—the thinnest possible crystal that can host such dislocations—by combining dark-field TEM and atomistic simulations. In contrast to dislocations in monolayer graphene, the dislocations reported here are real line defects confined between the two graphene layers. By applying Burgers vector analysis, we unambiguously identify the dislocations as partial dislocations with  $b = (1/3)\langle 1\bar{1}00\rangle$ , causing a change of the local stacking from AB to AC, and vice versa. The absence of stacking-fault energy, a unique peculiarity of bilayer graphene, gives rise to a characteristic equidistant arrangement of dislocations with alternating Burgers vectors

observed in large sample areas. One outcome of this study is that pronounced buckling of the bilayer graphene membrane at the dislocations enables the partial compensation of the normal strain and, surprisingly, the complete delocalization of the respective residual compressive and tensile strains in the two graphene layers. This makes the dislocations in freestanding bilayer graphene distinctly different from corresponding ones in graphite or other 3D crystals. In contrast to recent publications on strain solitons<sup>17</sup> and stacking-fault boundaries<sup>20</sup> based on observations in graphene grown by CVD, in our treatment of the investigated one-dimensional topological defects in bilayer graphene we consistently use the well-established concept of dislocations in crystalline solids and extend it to quasi-2D crystals.

We expect our findings to contribute to our understanding of basalplane dislocations and their role in tailoring the mechanical and electronic properties of bilayer and few-layer graphene. Our observation that such dislocations are already present in the initial epitaxial graphene on SiC will help explicate the restrictions on the transport properties of



this high-quality graphene material and should stimulate further studies on the local defect structure and related changes in the electronic properties. Furthermore, we anticipate that our freestanding bilayer graphene membranes with a well-defined distribution of parallel partial dislocations are good candidates for fundamental studies on (anisotropic) electronic transport in bilayer graphene and its potential use in future applications.

### **METHODS SUMMARY**

The investigated graphene membranes were prepared from high-quality epitaxial graphene on 6H-SiC according to a procedure recently described<sup>10</sup>. State-of-theart scanning electron microscopy (SEM) and aberration-corrected TEM including electron diffraction were used to investigate the local microstructure of the membranes, for example the distribution of graphene layers and their local stacking, as well as the extended network of basal-plane dislocations in the bilayer graphene. To confirm the local number of graphene layers, rocking curves of respective membrane regions (bi-, tri- and four-layer graphene) were determined from {1120} dark-field tilt series. In particular, the specific properties of the observed partial dislocations, such as Burgers vector, dislocation type and strain-field distribution, were examined in detail by a systematic dark-field analysis. To prove the local buckling (expected from our simulations) as well as the associated strain redistribution at the dislocation cores, the experimental data were quantitatively compared to simulated dark-field TEM images. Those TEM image simulations were based on atomic configurations of the partials, which we derived from calculations using atomistic interatomic potentials. To reproduce the periodic arrangement of alternating partials as observed in our bilayer graphene in the calculations, we used a rectangular periodic (185  $\times \sqrt{3}$ ) supercell that finally comprises two partials with alternating Burgers vectors (same edge components, opposite screw components). Furthermore, in the geometry optimization the atoms were either allowed to relax freely in all directions or were restricted to the x–y plane to reveal the pronounced effect of dislocation-induced buckling on the strain state of the membrane. From those configurations, the local atomistic strain, the disregistry between the two graphene layers, and the Burgers vector distributions for the edge and screw components of the partials were derived by evaluating the displacements of the carbon atoms.

Online Content Any additional Methods, Extended Data display items and Source Data are available in the online version of the paper; references unique to these sections appear only in the online paper.

## Received 28 May; accepted 14 October 2013. Published online 18 December 2013.

- Mott, N. F. Dislocations and the theory of solids. Nature 171, 234-237 (1953).
- Orowan, E. Zur Kristallplastizität. III. Über den Mechanismus des Gleitvorganges. Z. Phys. 89, 634–659 (1934).
- Taylor, G. I. The mechanism of plastic deformation of crystals. Part II. Comparison with observations. Proc. R. Soc. A 145, 388-404 (1934).
- Cottrell, A. H. & Bilby, B. A. Dislocation theory of yielding and strain ageing of iron. Proc. Phys. Soc. A 62, 49-62 (1949)
- Frank, F. & Read, W. Multiplication processes for slow moving dislocations. Phys. Rev. 79, 722-723 (1950).
- Nabarro, F. R. N. Mathematical theory of stationary dislocations. Adv. Phys. 1, 269-394 (1952)
- Shockley, W. Dislocations and edge states in the diamond crystal structure. Phys. Rev. 91, 228 (1953).
- Smoluchowski, R. Dislocations in ionic crystals (structure, charge effects and interaction with impurities). J. Phys. Collog. 27, C3 (1966).
- Hull, D. & Bacon, D. J. Introduction to Dislocations (Pergamon, 2001).

- 10. Waldmann, D. et al. Robust graphene membranes in a silicon carbide frame. ACS Nano 7, 4441-4448 (2013).
- 11. Bao, W. et al. Stacking-dependent band gap and quantum transport in trilayer graphene. Nature Phys. 7, 948-952 (2011).
- Lui, C. H., Li, Z., Mak, K. F., Cappelluti, E. & Heinz, T. F. Observation of an electrically tunable band gap in trilayer graphene. *Nature Phys.* **7**, 944–947 (2011).

  13. Wong, J.-H., Wu, B.-R. & Lin, M.-F. Strain effect on the electronic properties of single
- layer and bilayer graphene. J. Phys. Chem. C 116, 8271-8277 (2012).
- Vaezi, A., Liang, Y., Ngai, D. H., Yang, L. & Kim, E.-A. Topological edge states at a tilt
- boundary in gated multilayer graphene. *Phys. Rev. X* **3**, 021018 (2013). 15. Amelinckx, S. & Delavignette, P. Observation of dislocations in non-metallic layer structures. Nature 185, 603-604 (1960).
- Delavignette, P. & Amelinckx, S. Dislocation patterns in graphite. J. Nucl. Mater. 5, 17-66 (1962).
- Alden, J. S. et al. Strain solitons and topological defects in bilayer graphene. Proc. Natl Acad. Sci. USA **110**, 11256–11260 (2013).
- 18. Brown, L. et al. Twinning and twisting of tri- and bilayer graphene. Nano Lett. 12, 1609-1615 (2012).
- 19. Hattendorf, S., Georgi, A., Liebmann, M. & Morgenstern, M. Networks of ABA and ABC stacked graphene on mica observed by scanning tunneling microscopy. Surf. Sci. 610, 53-58 (2013).
- Lin, J. et al. AC/AB stacking boundaries in bilayer graphene. Nano Lett. 13, 3262-3268 (2013).
- Shevitski, B. et al. Dark-field transmission electron microscopy and the Debye-Waller factor of graphene. Phys. Rev. B 87, 045417 (2013).
- Ping, J. & Fuhrer, M. S. Laver number and stacking sequence imaging of few-laver graphene by transmission electron microscopy. Nano Lett. 12, 4635-4641
- 23. Meyer, J. C. et al. The structure of suspended graphene sheets. Nature 446, 60-63 (2007).
- Warner, J. H. et al. Dislocation-driven deformations in graphene. Science 337, 209-212 (2012).
- Lehtinen, O., Kurasch, S., Krasheninnikov, A. V. & Kaiser, U. Atomic scale study of the life cycle of a dislocation in graphene from birth to annihilation. Nature Commun. 4, 2098 (2013).
- Yazyev, O. V. & Louie, S. G. Topological defects in graphene: dislocations and grain boundaries. Phys. Rev. B 81, 195420 (2010).
- 27. Chen, S. & Chrzan, D. C. Continuum theory of dislocations and buckling in graphene. Phys. Rev. B 84, 214103 (2011).
- Eshelby, J. D. & Stroh, A. N. CXL. Dislocations in thin plates. Phil. Mag. 42, 1401-1405 (1951).
- Siems, R., Delavignette, P. & Amelinckx, S. The buckling of a thin plate due to the presence of an edge dislocation. Phys. Status Solidi B 2, 421-438 (1962)

**Supplementary Information** is available in the online version of the paper.

Acknowledgements We acknowledge use of experimental equipment of P. Schmuki. Furthermore, we thank J. Müller, E. Bitzek and A. Kohlmeyer for discussions. This research was supported by the Deutsche Forschungsgemeinschaft within the frameworks of the SFB 953 'Synthetic Carbon Allotropes' and the Cluster of Excellence  ${\it EXC~315~`} Engineering~of~Advanced~Materials'~at~the~Friedrich-Alexander-Universit\"{a}t$ Erlangen-Nürnberg

Author Contributions B.B. and E.S. designed the experiments. D.W. and C.D. prepared the membranes based on the route recently developed and optimized by D.W., H.B.W. and B.B. B.B. and C.D. conducted the TEM experiments. B.B., E.S. and C.D. evaluated the experimental data. K.W. and B.M. performed the atomistic simulations. F.N. simulated the TEM dark-field images and rocking curves (using the atomistic configurations from K.W. and B.M.). Furthermore, F.N. determined the 2D strain and derived the Burgers vector distributions. B.B. and E.S. wrote the manuscript. All authors discussed the results and implications and commented on the manuscript at all stages

Author Information Reprints and permissions information is available at www.nature.com/reprints. The authors declare no competing financial interests. Readers are welcome to comment on the online version of the paper. Correspondence and requests for materials should be addressed to B.B. (benjamin.butz@ww.uni-erlangen.de) or E.S. (erdmann.spiecker@ww.uni-erlangen.de).



#### **METHODS**

**Sample preparation.** The graphene membranes have been prepared from high-quality quasi-freestanding graphene on 6H-SiC according to the elaborated procedure recently described by the authors<sup>10</sup>.

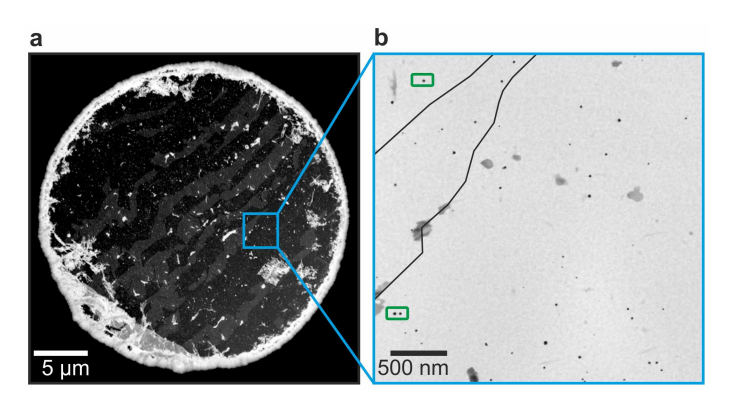
Electron microscopy. Scanning electron microscopy (SEM) in transmission is conducted using a Zeiss Supra microscope (high tension 10 kV). Aberration-corrected HRTEM, BF/DF TEM and electron diffraction are performed using a FEI Titan<sup>3</sup> 80-300 microscope. It was operated at 80 kV to prevent electron-beam-induced damaging of the graphene membranes<sup>30</sup>. For centred dark-field imaging (exposure time, 60 s) an aperture with a radius corresponding to 0.065 mrad was used. It has to be mentioned here that all dark-field images are unprocessed except for histogram stretching (constant black level). The rocking curves were derived by evaluating the dependencies of the local {1120} dark-field image mean intensity on tilt angle. Therefore, suitable areas in bi-, tri- and 4-layer graphene were selected (Extended Data Fig. 2, Supplementary Video 1). The TEM sample was azimuthally aligned within the TEM sample holder with  $\{11\overline{2}0\}$  lattice planes parallel to the tilt axis of the goniometer, that is, a  $\{11\overline{2}0\}$  reflection perpendicular to the tilt axis. Theoretical rocking curves for an equilibrium interlayer distance of 3.370 Å were calculated according to kinematic diffraction theory. Damping due to the atomic scattering factor of carbon<sup>31</sup> and the Debye-Waller factor<sup>32</sup> (mean square displacement of 40 pm<sup>2</sup>) were taken into account. Using the atomistic models, dark-field TEM images were simulated by multislice calculation (TEMSIM package + application of dark-field aperture/microscope transfer function<sup>31</sup>). The modulus of the secondorder derivative of the experimental and the theoretical dark-field images was calculated by applying the Hessian matrix (maximal values) subsequently to Gaussian smoothing (width of 1.5 pixels in the experimental images, corresponding to 1.7 nm) using FEATUREJ (ImageJ plugin by E. Meijering).

**Modelling.** The atomistic simulations were performed with the LAMMPS molecular dynamics simulator software package<sup>33</sup>. AIREBO<sup>34</sup> and a registry-dependent interlayer potential<sup>35</sup> were used to model the in-plane covalent carbon bonds and interlayer interactions in bilayer graphene, respectively. With this set-up, we obtain an in-plane carbon–carbon distance of 1.399 Å. The equilibrium separation for two planar graphene layers in AB stacking (not allowing a buckling of the layers) is

3.370 Å, and the cohesion energy amounts to 45.0 meV per atom with respect to one graphene layer (cleavage energy per atom). Details of the resulting gamma surface are presented in Extended Data Fig. 5. For the simulations of the dislocation structures, periodic boundary conditions were applied in the plane of the bilayer by using a rectangular supercell with dimensions of 185 and  $\sqrt{3}$  times the graphene lattice constant (2.423 Å) in the x and y directions, respectively. One perfect dislocation with its Burgers vector  $b = (1/3)[11\bar{2}0]$  parallel to the x axis was introduced by adding four more atoms in the top layer. To accommodate the additional atoms, either one or two sinusoidal height modulations were imprinted into the bilayer. Structural relaxation of both initial configurations, which included optimization of the unit-cell dimensions, gave the same result of an equidistant pair of partials.

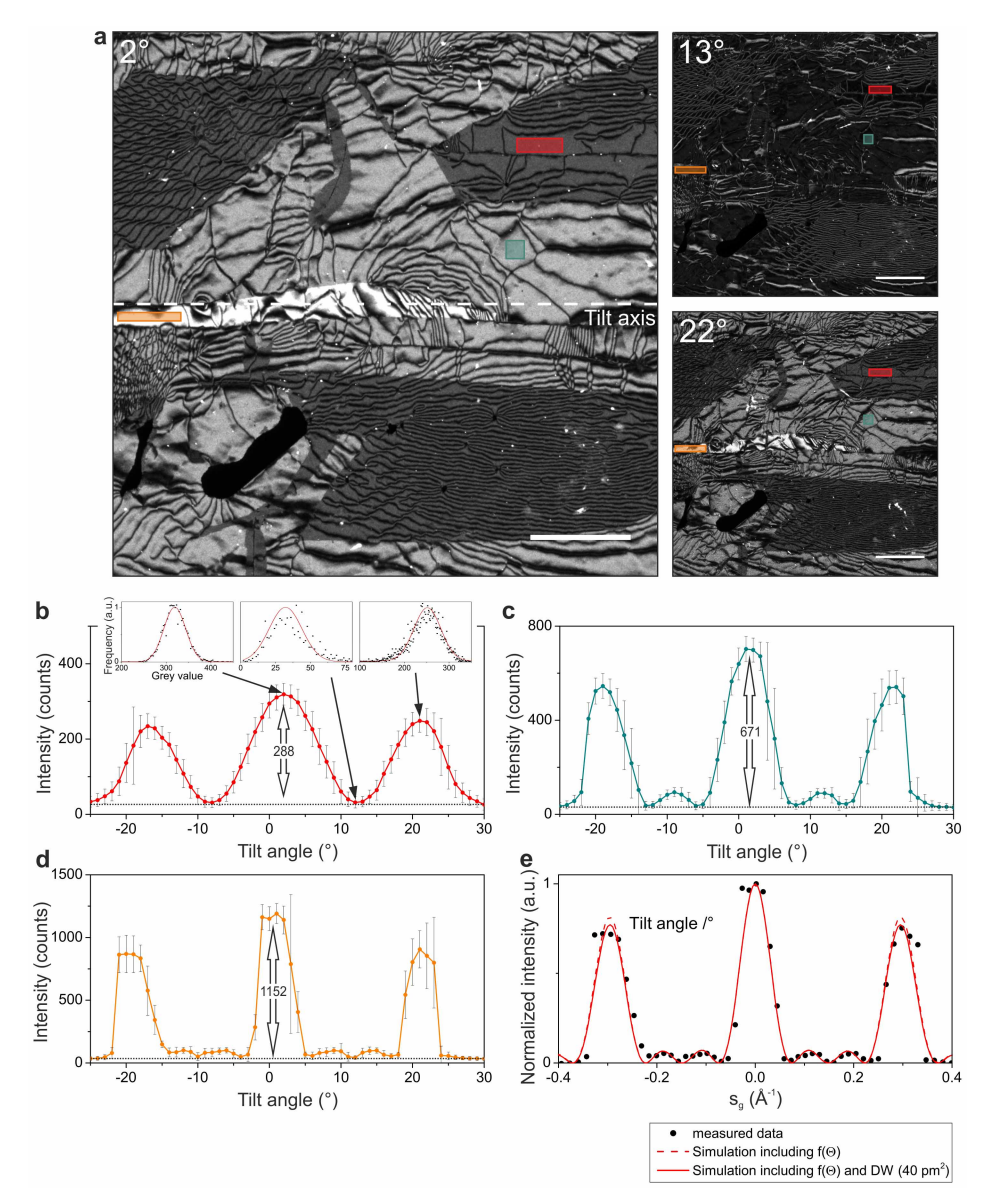
The analysis of the strain distribution was done separately for the two graphene layers. The atomic displacements were converted into local strains by using the concept of local atomistic strain³6. At each atom, a local 2D coordinate system, tangential to the buckled graphene layers, is introduced. The local strain is determined with respect to the reference configuration of an undistorted graphene monolayer from the changes of the vectors connecting nearest-neighbour atoms. The disregistry function and its derivative, the Burgers vector distribution, of the screw and edge dislocation components were calculated from the normal vectors to the same local coordinate system used for the strain analysis.

- Meyer, J. C. et al. Accurate measurement of electron beam induced displacement cross sections for single-layer graphene. Phys. Rev. Lett. 108, 196102 (2012).
- 31. Kirkland, E. J. *Advanced Computing in Electron Microscopy* (Springer, 2010).
- Tewary, V. & Yang, B. Singular behavior of the Debye-Waller factor of graphene. Phys. Rev. B 79, 125416 (2009).
- Plimpton, S. Fast parallel algorithms for short-range molecular dynamics. J. Comput. Phys. 117, 1–19 (1995).
- Brenner, D. W. et al. A second-generation reactive empirical bond order (REBO) potential energy expression for hydrocarbons. J. Phys. Condens. Matter 14, 783–802 (2002).
- Kolmogorov, A. & Crespi, V. Registry-dependent interlayer potential for graphitic systems. *Phys. Rev. B* 71, 235415 (2005).
- Shimizu, F., Ogata, S. & Li, J. Theory of shear banding in metallic glasses and molecular dynamics calculations. *Mater. Trans.* 48, 2923–2927 (2007).



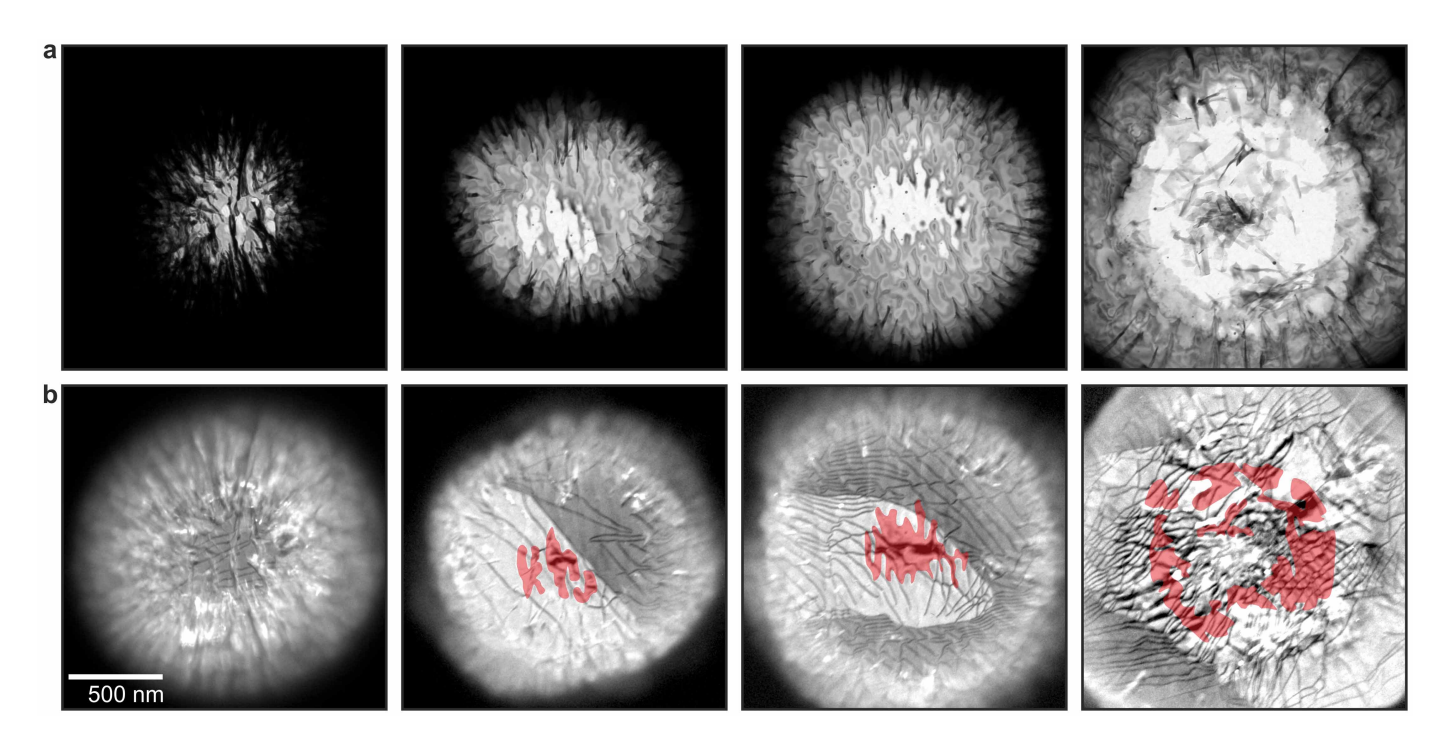
## Extended Data Figure 1 | Overview of the investigated membrane.

**a**, Transmission SEM image of the investigated membrane, from which the TEM images in **b** and Figs 2 and 3 were obtained. The blue square indicates the studied region. **b**, Bright-field image corresponding to Figs 2 and 3. The green rectangles mark residual nanoparticles as guides to the eye. They are also visible in the dark-field images in Fig. 2.



Extended Data Figure 2 | Dark-field tilt-series acquisition and determination of rocking curves. a, Example images (tilt angles given) of the  $\{11\bar{2}0\}$  dark-field tilt series recorded with the tilt axis (horizontally aligned) perpendicular to the  $\{11\bar{2}0\}$  reflection. The complete series is available as Supplementary Video 1. The direct tracking of the shape amplitude of the membrane leads to drastic changes of the measured  $\{11\bar{2}0\}$  intensities depending on the tilt angle. The scale bar corresponds to  $500 \, \mathrm{nm}$ .  $\mathbf{b}$ – $\mathbf{d}$ , Rocking

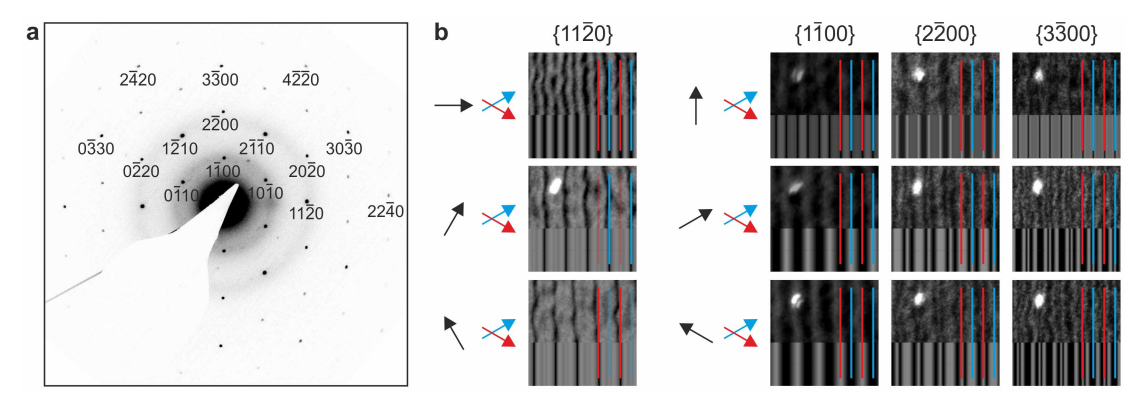
curves for 2, 3 or 4 layers of graphene derived from the regions marked by the coloured rectangles by measuring the local mean intensities in every image, that is, for every tilt angle. The given tilt angles are not corrected for any pre-tilt causing the slight shifts of the intensity distributions (see position of central maximum). e, Normalized rocking curve of 4-layer graphene in comparison to our simulation taking into account damping due to the atomic scattering factor and thermal vibrations (Debye–Waller factor) (solid line).



Extended Data Figure 3 | On the origin of the dislocations. Series of related bright-field (a) and  $\{11\bar{2}0\}$  dark-field (b) images of small holes at early stages of etching: size of freestanding membranes increases from left to right (compare with the bright-field images in a). Blocking the intensity contributions from the SiC in  $\{11\bar{2}0\}$  dark-field imaging by using an adequate objective aperture allows for the defect characterization of the

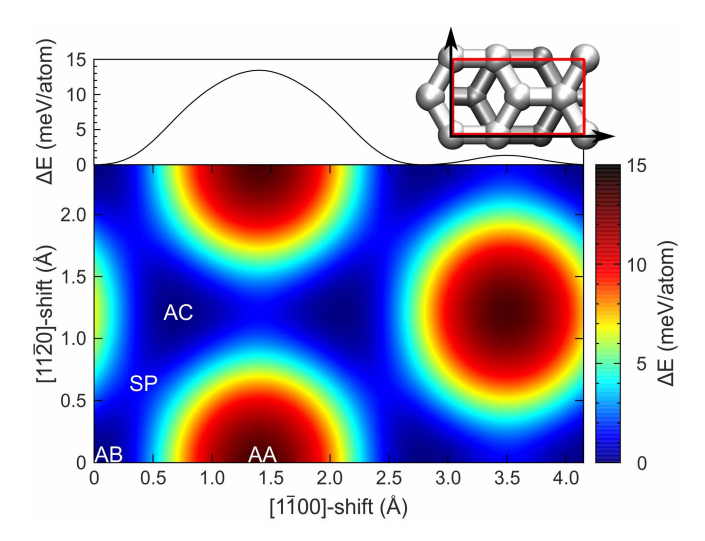
graphene even in wide regions, where the SiC has not been removed by the wet chemical etching. The area of the freestanding graphene (derived from a), where the SiC is already gone, is marked in red in the dark-field images. All dark-field images indicate a high density of dislocations in the observable region around each hole.



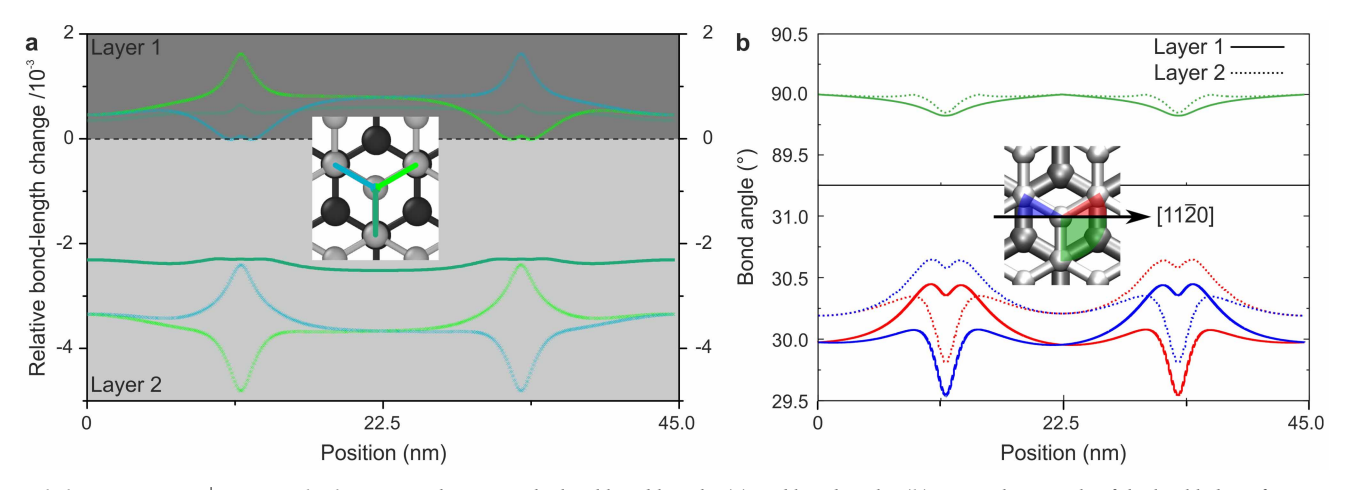


**Extended Data Figure 4** | **Experiment versus simulation.** a, b, Compilation of dark-field images (b) obtained with outer reflections (as indicated in a). Following our depiction in Fig. 3, the respective directions of the active reflection (black arrows) and the Burgers vectors (red, blue arrows and lines)

are given. For comparison, the simulated dark-field intensity distributions, obtained from the buckled atomistic configuration (compare with Fig. 4), are shown as insets. These are in very good agreement with the measured data.



Extended Data Figure 5 | Gamma surface. Calculated unrelaxed gamma surface of ideal planar bilayer graphene on sliding the two planes at the equilibrium interlayer distance of 3.370 Å. The ideal AB stacking is taken as the zero-point of energy and the energy differences,  $\Delta E$ , on lateral displacement of one graphene layer are given per atom of one graphene layer. The upper inset depicts a cut through the gamma surface along the crystallographic [1100] axis, illustrating the energy profile along a path leading from AB to AA, AC, SP and back to AB stacking. The SP and AA barrier heights are 1.4 meV per atom and 13.5 meV per atom, respectively. For comparison: a simple Lennard–Jones van der Waals potential, which has been parameterized to give the same cohesive energy (45.0 meV per atom) and equilibrium layer separation (3.370 Å) for AB stacking, would yield SP and AA barriers of only 0.1 meV per atom and 0.8 meV per atom, respectively.



**Extended Data Figure 6** | **Structural relaxation.** Changes in the local bond lengths (a) and bond angles (b) across the partials of the buckled configuration (compare with Fig. 4).